Thermal and mechanical characterizations of a substrate-free focal plane array*

Cheng Teng(程 腾)[a], Zhang Qing-Chuan(张青川)[a]†, Chen Da-Peng(陈大鹏)[b], Shi Hai-Tao(史海涛)[a], Gao Jie(高 杰)[a], Qian Jian(钱 剑)[a], and Wu Xiao-Ping(伍小平)[a]

[a] *CAS Key Laboratory of Mechanical Behavior and Design of Materials, University of Science and Technology of China, Hefei* 230027, *China*

[b] *Institute of Microelectronics, Chinese Academy of Science, Beijing* 100029, *China*

(Received 20 March 2009; revised manuscript received 18 May 2009)

We propose a substrate-free focal plane array (FPA) in this paper. The solid substrate is completely removed, and the microcantilevers extend from a supporting frame. Using finite element analysis, the thermal and mechanical characterizations of the substrate-free FPA are presented. Because of the large decrease in thermal conductance, the supporting frame is temperature dependent, which brings out a unique feature: the lower the thermal conductance of the supporting frame is, the higher the energy conversion efficiency in the substrate-free FPA will be. The results from the finite element analyses are consistent with our measurements: two types of substrate-free FPAs with pixel sizes of 200×200 and 60×60 μm^2 are implemented in the proposed infrared detector. The noise equivalent temperature difference (NETD) values are experimentally measured to be 520 and 300 mK respectively. Further refinements are considered in various aspects, and the substrate-free FPA with a pixel size of 30×30 μm^2 has a potential of achieving an NETD value of 10 mK.

Keywords: focal plane array, infrared detectors, substrate-free, uncooled
PACC: 0710C, 0762, 4410

1. Introduction

Infrared (IR) is the second most intense radiation band in our environment, its detection and imaging have extensive applications in industrial, military, and commercial fields.[1,2] Up to now, different types of IR detectors have been developed. They are broadly grouped into two main categories: photon (cooled) and thermal (uncooled).[3] In photon detectors the radiation is absorbed within the material by the interaction between electrons either bound to lattice atoms or to impurity atoms or between free electrons. The observed electrical output signal results from the change of electronic energy distribution. Photon detectors typically exhibit both perfect signal-to-noise performance and a very fast response. But cooling requirements are the main obstacle to more extensive applications. In contrast, thermal detectors operate based on a simple principle, i.e. when the detectors are heated by incoming IR radiation their temperature increases and the temperature change can be measured by any temperature-sensitive mechanism, such as thermoelectric voltage, resistance, pyroelectric voltage.

In recent years, advances in micro-electro-mechanical systems (MEMS) have led to the development of thermal detectors operating as microcantilever ones.[3] The microcantilever deflection induced by the temperature change is measured by various readout schemes, such as capacitive, piezoresistive, and optical readout schemes. Researchers have designed a number of architectures in the development of IR FPAs.[4−10] But traditionally all types of FPAs are substrate arrays, that is, the microcantilevers are typically suspended on a solid silicon (Si) substrate with a gap of 2–3 μm. This solid substrate is usually considered to be a temperature-independent one due to its high heat capacity, and each microcantilever functions independently. Such a design brings out a common issue about the energy conversion efficiency H, defined as the temperature change of microcantilevers $\Delta T_{\rm C}$ due to the temperature change of IR sources $\Delta T_{\rm S}$: when researchers reduce the pixel size to achieve some potential benefits, such as a higher spatial resolution, the energy conversion efficiency will decrease so sharply that the detector sensitivity is seriously limited. Based on the deductions of Zhao *et*

*Project supported by the National Natural Science Foundation of China (Grant Nos. 10732080 and 10627201), and the National Basic Research Program of China (Grant No. 2006CB300404).
†Corresponding author. E-mail: zhangqc@ustc.edu.cn
© 2010 Chinese Physical Society and IOP Publishing Ltd

al.[9] the energy conversion efficiency would decrease from 6% to 0.2% when the pixel size changes from 110 to 25 μm. Although there are some ways to improve the energy conversion efficiency, such as using the strategy of resonance cavity, the overall level of fabrication complexity reported previously has enormously increased.

We proposed a substrate-free FPA that involves only several simple fabrication steps in 2004.[11] The solid substrate has been completely removed and the microcantilevers extend from a supporting frame. Up to now, several batches of such an FPA with different pixel sizes have been fabricated successfully.[11−14] When they are implemented in the proposed IR detector with optical readout, the detector sensitivity increases with the decrease of pixel size. This tendency of change in sensitivity is quite contrary to a conventional understanding of the substrate FPA. Therefore, this work attempts to analyse and demonstrate the thermal and mechanical characterizations of the substrate-free FPA. Using finite element analysis, some figures of merit commonly used in the field are estimated. Meanwhile in order to reveal the advantages of the substrate-free FPA, characterizations of the substrate FPA have also been conducted.

2. Design and fabrication

The geometry of a single pixel (microcantilever) of the substrate-free FPA is illustrated in Fig. 1. Each pixel, extending from a supporting frame, consists of an IR absorber (or reflector), temperature-dependent bimaterial regions, and thermal isolation regions. Here, the IR absorber is designed to provide both absorption of the radiation and the reflection of the probing light, and bimaterial regions are folded to accommodate a larger deflection angle of the IR absorber.

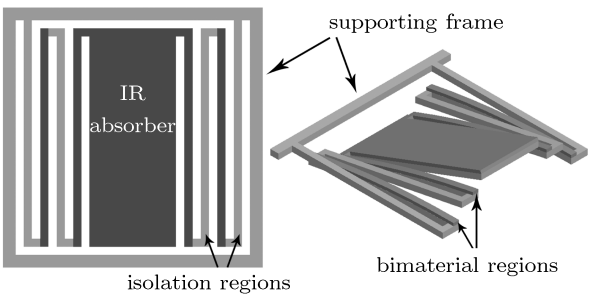


Fig. 1. Geometry of a single pixel (microcantilever) of the substrate-free FPA.

Figure 2 shows the basic fabrication steps of the substrate-free FPA. (a) It starts with a double side polished Si wafer with a thickness of 300 μm. (b) Two low stress SiN_x films are then deposited on the double sides of the Si wafer by low pressure chemical vapour deposition (LPCVD). (c) Then the inductively coupled plasma (ICP) etching is used to pattern a wet-etching window on the backside of the Si wafer. (d) On the front side, the ICP etching is used again to pattern the SiN_x geometry. (e) Lift-off technology is followed to form the two-fold interval-metalized architecture. In order to decrease the undesired deformations in the IR absorber, only a 50 Å Au layer is deposited here. (f) The final step is to remove the Si substrate by using wet etching. It is notable that the overall level of the fabrication complexity is significantly low as compared with that of the fabrications reported previously.

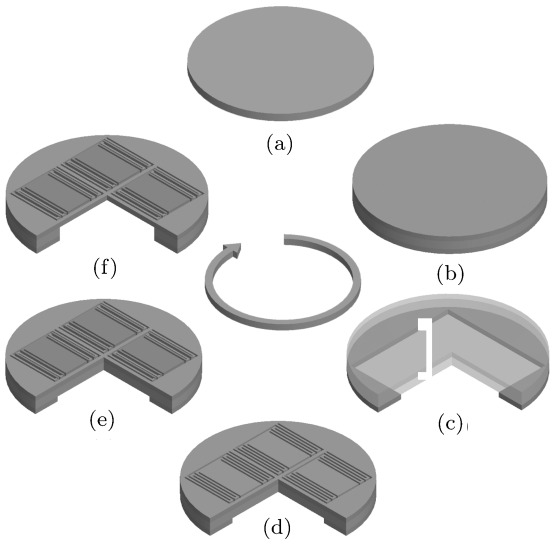


Fig. 2. Basic fabrication steps of the substrate-free FPA. (a) It starts with a double side polished Si wafer. (b) Two low stress SiN_x films are then deposited on the double sides by low pressure chemical vapour deposition (LPCVD). (c) Then inductively coupled plasma (ICP) etching is used to pattern a wet-etching window on the backside of the Si wafer. (d) On the front side, ICP etching is used again to pattern the SiN_x geometry. (e) The lift-off technology is followed to form the two-fold interval-metalized architecture. (f) The final step is to remove the Si substrate by using wet etching.

3. Thermal and mechanical characterizations

In order to gain an insight into the performance of the substrate-free FPA, finite element analysis is

utilized to simulate the thermal and mechanical characterizations.

As a thermal detector, the microcantilevers are not always in a thermal equilibrium state. The transient characteristic therefore plays an especially important role in investigating the performance of the substrate-free FPA. However, in the uncooled IR detectors, the microcantilevers are always installed to function in the thermal equilibrium state for high quality thermal images, namely, the sampling time of the IR detector must be longer than the thermal response time τ of microcantilevers. In the author's work, the substrate-free FPA generally functions with a sampling time of 40 ms (25 frames/s for the real time thermal video). Therefore, in the present paper the thermal response time τ is used to give a rough understanding of the transient characteristic, and our attention is mainly paid to the steady-state analysis.

A simplified analysis of the temperature of microcantilevers, which does not require knowledge of the microcantilever mechanism, was performed.[15] Considering the IR system to be initially at ambient temperature T_0 (=298 K) and the incident heat flux q (10 pW/μm^2), the temperature of microcantilevers $T_{\rm C}$ will follow[16]

$$\rho V c\frac{{\rm d}T_{\rm C}}{{\rm d}t} = -G_{\rm all}(T_{\rm C} - T_0) + Aq, \qquad (1)$$

where ρ is the density of material, V the volume of microcantilevers, c the heat capacity, A the effective absorbing area, and $G_{\rm all}$ the total thermal conductance, which contains primarily two parts: (1) heat transfer path, delivering from the microcantilevers to the supporting frame. Namely, the microcantilevers and the supporting frame are connected in series in the thermal circuit, and the thermal conductances of the microcantilevers $G_{\rm can}$ and the supporting frame $G_{\rm frm}$ therefore can be equivalent to a parallel connection; (2) heat loss through radiation $G_{\rm rad}$. Heat loss through convection can be neglected for the vacuum environment ($\leq$ 1 Pa).[17] Namely, the total thermal conductance $G_{\rm all}$ can be expressed as

$$G_{\rm all} = \frac{G_{\rm can}G_{\rm frm}}{G_{\rm can} + G_{\rm frm}} + G_{\rm rad}. \qquad (2)$$

It is notable that the selection of the incident heat flux is based on a typical temperature variation of about 20 K for the IR sources at room temperature. According to the proposed IR system, the incident heat flux q can be expressed as[16,18]

$$q = \frac{\zeta\varepsilon\pi}{4F_{\rm no}^2}\cdot\Delta T_{\rm S}\cdot\left(\frac{{\rm d}P}{{\rm d}T_{\rm S}}\right)_{8-14\ \mu{\rm m}}, \qquad (3)$$

where ζ is the optical transmissivity of the IR system (= 0.9), ε the total emissivity of the material (=0.81), $F_{\rm no}$ the F-number of the IR lens (=0.8), $T_{\rm S}$ the temperature of the IR source, and $({\rm d}P/{\rm d}T_{\rm S})_{8-14\ \mu{\rm m}}$ is a fraction of the radiative energy emitted by a blackbody target within the spectral band from 8 to 14 μm (=0.63 W$\cdot$m$^{-2}\cdot$K$^{-1}\cdot$sr^{-1}). Based on an incident heat flux of 10 pW/μm^2, the temperature variation of IR sources $\Delta T_{\rm S}$ will be estimated to be about 18 K.

When the IR system is in thermal equilibrium with the surroundings, the transient part of Eq. (1) can be eliminated, and the temperature change of microcantilevers $\Delta T_{\rm C}$ would be

$$\Delta T_{\rm C} = T_{\rm C} - T_0 = \frac{Aq}{\dfrac{G_{\rm can}G_{\rm frm}}{G_{\rm can} + G_{\rm frm}} + G_{\rm rad}}. \qquad (4)$$

Hence, it becomes obvious that $\Delta T_{\rm C}$, as a function of $G_{\rm frm}$, will increase with the decrease of $G_{\rm frm}$.

Based on the above analyses, and using the material properties and structural parameters in Table 1 and Table 2, the three-dimensional (3-D) finite element model (FEM) with 80×80 pixels was developed. The steady-state thermal analysis of the substrate-free FPA was performed. Meanwhile, in order to reveal the advantages of the substrate-free FPA, steady-state thermal analysis of the substrate FPA was also conducted. Here, the substrate FPA means that the geometry of the FPA is just the same as the substrate-free FPA, but the supporting frame (or the Si substrate) is considered to be a temperature-independent one. Two kinds of thermal loads were designed in the present paper.

Table 1. Material properties of the finite element models used.

material	density $\rho/(10^3{\rm kg\cdot m^{-3}})$	Young's modulus E/GPa	expansion coeff. $\alpha/10^{-6}$ K^{-1}	thermal cond. $k/({\rm W\cdot m^{-1}\cdot K^{-1}})$	heat capacity $c/({\rm J\cdot kg^{-1}\cdot K^{-1}})$	emissivity ε
SiN_x	2.40	180	0.8	5.5	691	0.8
Au	19.3	73	14.2	296	129	0.01

Table 2. Structural parameters of the finite element models used.

model No.	pixel size /μm^2	absorber size /μm^2	supporting frame width /μm	leg width /μm	Au layer thickness /μm	SiN_x layer thickness /μm
1	200×200	180×130	10	2	0.2	2
2	60×60	53×21	3	2	0.2	0.3
3	30×30	28×20	1	0.5	0.2	0.3

3.1. The first kind of thermal load

For each FEM in Table 2, the heat flux (10 pW/μm^2) was used on only one pixel to evaluate the performance of the substrate-free FPA. As an example, Fig. 3 shows a close-up of the obtained temperature distribution in FEM 2 (with a pixel size of 60×60 μm^2). The temperature change $\Delta T_{\rm C}$ due to the pixel absorbing heat flux is 0.32 K, increased by about 28% as compared with the temperature change $\Delta T_{\rm C}$ of 0.25 K in the substrate FPA.

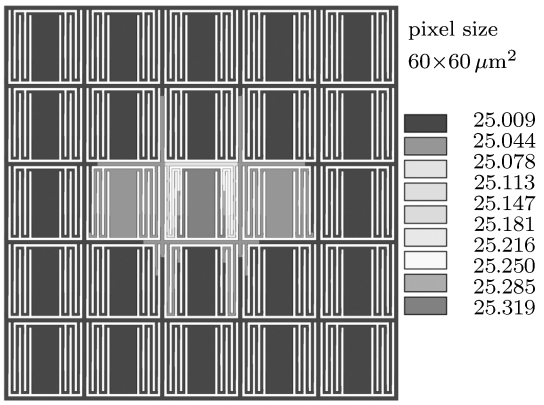


Fig. 3. Close-up of the temperature distribution (in units of °C caused by the heat flux (10 pW/μm^2) over one pixel of FEM 2 (with a pixel size of 60×60 μm^2).

This simulation result is consistent with expression (4).

For the substrate FPA, the supporting frame (or the Si substrate) is considered to be a temperature-independent one, that is, $G_{\rm frm} = +\infty$ and $G_{\rm all}$ can be simplified into

$$G_{\rm all} = G_{\rm can} + G_{\rm rad}. \tag{5}$$

Based on the deductions in Ref. [13] and [14], $G_{\rm can}$ and $G_{\rm rad}$ can be expressed as

$$G_{\rm can} = 2\left(\frac{nL_{\rm Leg}}{k_{{\rm SiN}_x}A_{{\rm SiN}_x} + k_{\rm Au}A_{\rm Au}} + \frac{nL_{\rm Leg}}{k_{{\rm SiN}_x}A_{{\rm SiN}_x}}\right)^{-1}, \tag{6}$$

$$G_{\rm rad} = 4\sigma A_{\rm ab}(\varepsilon_{\rm Au} + \varepsilon_{{\rm SiN}_x})T_{\rm C}^3, \tag{7}$$

where n is the multi-fold number (=2), $A_{{\rm SiN}_x}$ the cross sectional area of the SiN_x leg, $A_{\rm Au}$ the cross sectional area of the Au leg, k the thermal conductivity of the material, $L_{\rm Leg}$ the leg length that equals the length of the absorber, σ the Stefan–Boltzmann constant (=5.67×10^{-8} W·m^{-2}·K^{-4}), and $A_{\rm ab}$ the area of the absorber. Therefore, the temperature change $\Delta T_{\rm C}$ in the substrate FPA can be calculated to be 0.17 K. This analytical calculation is consistent with the simulation result of 0.25 K, and the discrepancy between them can be attributed to the neglect of both absorption and radiation of the legs in expression (6).

For the substrate-free FPA, the supporting frame is a temperature-dependent structure (shown in Fig. 3). Namely, $G_{\rm frm} \neq +\infty$ and exactly due to its contribution, the temperature change $\Delta T_{\rm C}$ in the substrate-free FPA would be higher than that in the substrate FPA (increased by about 28% for FEM 2).

3.2. The second kind of thermal load

It is notable that there is temperature pre-change in the neighbours without absorbing heat flux (Fig. 3). This means that the temperature change of each microcantilever in the substrate-free FPA will be dependent on both the IR absorption induced by itself and the linear superposition of the temperature pre-change induced by the neighbours. This thermal characteristic could significantly increase the temperature change and therefore improve the performance. This inference is supported by the following finite element analysis.

Considering that there are usually groups of pixels simultaneously absorbing IR radiation, 3.6 μW (10 pW/μm^2) heat flux was applied to the central area of the FEMs. For the pixel sizes of 200×200, 60×60, and 30×30 μm^2, the numbers of the microcantilevers absorbing heat flux can thus be calculated to be 9, 100, and 400 pixels respectively. The temperature distributions obtained in such situations are shown in Fig. 4. Figure 5 shows close-ups of the temperature distributions in Figs. 4(a), 4(b) and 4(c). With the decrease of pixel size, the temperature change in the substrate FPA decreases sharply from 1.13 to 0.20 K. However, the temperature change in the substrate-free

FPA is nearly at the same level, changing from 1.19 to 1.55 K, and seems to bear no direct relation to pixel size. For the substrate FPA, the supporting frame (or the Si substrate) is considered to be a temperature-independent one, the microcantilevers therefore function independently, and there is no difference between the two kinds of thermal loads. Based on expressions (4)–(7), the values of temperature change $\Delta T_{\rm C}$ of 1.19, 0.25, and 0.20 K in the substrate FPA (shown in Figs. 4 (b), 4(d), and 4(f) can also be calculated to be 1.07, 0.17, and 0.18 K respectively. The discrepancies among them can be attributed to the neglect of both absorption and radiation of the legs in expression (6).

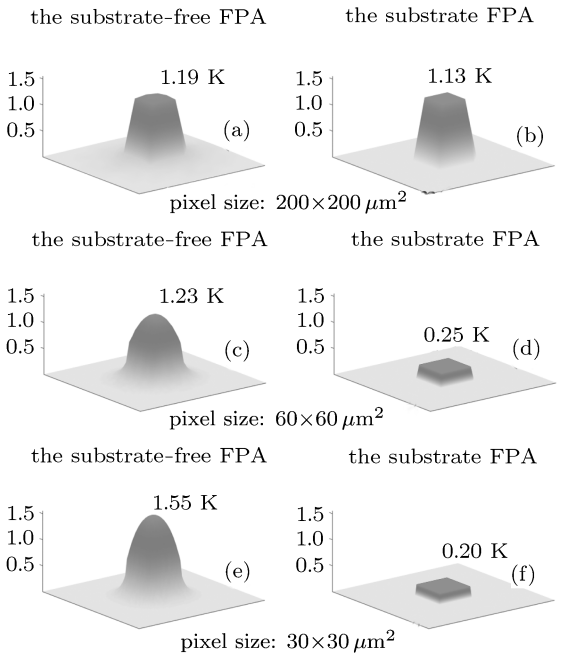


Fig. 4. Temperature distributions (in units of K) in [(a), (c), (e)] the substrate-free FPA and [(b), (d), (f)] the substrate FPA. The 3.6 μW (10 pW/μm^2) heat flux is applied to the central area of the models. For the pixel sizes of 200×200, 60×60, and 30×30 μm^2, the numbers of the microcantilevers absorbing heat flux can thus be calculated to be 9, 100, and 400 pixels respectively.

For the substrate-free FPA, the supporting frame is a temperature-dependent structure (shown in Fig. 5), the temperature change $\Delta T_{\rm C}$ of each microcantilever therefore comes from two parts: (i) the incident IR energy absorbed by itself. This portion of $\Delta T_{\rm C}$ can be evaluated by expressions (2) and (4); (ii) the linear superposition of the temperature pre-change induced by the neighbours. Hence, a significant increase in $\Delta T_{\rm C}$ can be achieved for the substrate-free FPA. As can be seen in Fig. 4, the values of $\Delta T_{\rm C}$ of 1.19, 1.23 and 1.55 K in the substrate-free FPA increase by about 0.05, 3.9 and 6.8 times those in the substrate FPA respectively. It is noticeable that the increment for FEM 1 is much less than those for FEM 2 and FEM 3 mainly because the thermal conductance of the supporting frame $G_{\rm frm}$ for FEM 1 is still relatively large (the cross sectional area of the supporting frame is 10×2 μm^2 for FEM 1, but 3×0.3, and 1×0.3 μm^2 for FEM 2 and FEM 3 respectively). As can be seen from Fig. 5(a), the average temperature change of the supporting frame is only about 0.35 K for FEM 1, therefore the thermal behaviour of FEM 1 is more similar to that of the substrate FPA.

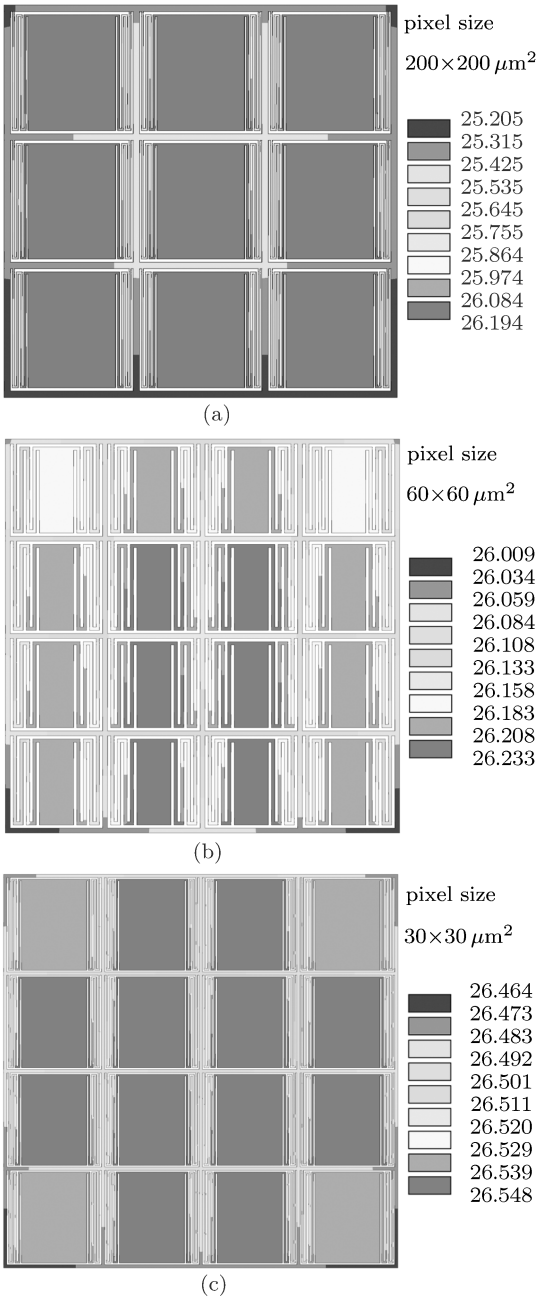


Fig. 5. Close-ups of the temperature distributions in units of °C in Figs. 4(a), 4(c), and 4(e). The temperature boundary condition is a constant temperature , i.e. 25 °C.

Finally, using the simulation results described above, some figures of merit commonly used in the field were estimated and listed in Table 3. The total thermal conductance $G_{\rm all}$ of each microcantilever is calculated to be

$$G_{\rm all} = \frac{A_{\rm ab} q}{\Delta T_{\rm C}}, \tag{8}$$

where the used data of $\Delta T_{\rm C}$ comes from the first kind of thermal load. The thermal response time τ is calculated to be

$$\tau = \frac{C}{G_{\rm all}}, \tag{9}$$

where C is the heat capacity of the IR absorber. Note that in order to function at least at 25 frames/s for the real-time thermal video, a response time of less than 40 ms is essential. Then a comparison of the energy conversion efficiency H between the substrate/substrate-free FPA was performed. Practically considering that there are usually groups of pixels simultaneously absorbing IR radiation, the temperature change $\Delta T_{\rm C}$ caused by the second kind of thermal load (as shown in Fig. 4) was utilized. The estimates in Table 3 indicate that the lower the thermal conductance of the supporting frame $G_{\rm all}$ is, the higher the energy conversion efficiency H in the substrate-free FPA will be. The decreasing trend in the substrate FPA, namely that the energy conversion efficiency decreases with decreasing pixel size, has been completely avoided. It is worth noting that the strategy of the substrate-free FPA is compatible with many other types of uncooled IR detectors.

Table 3. Some figures of merit commonly used in the field.

model No.	thermal conductance $G_{\rm all}$ /(W/K)	thermal response time τ /ms	energy conversion efficiency H	
			substrate-free FPA	substrate FPA
1	2.35×10^{-7}	330	6.6%	6.3%
2	3.49×10^{-8}	16	6.8%	1.4%
3	2.30×10^{-8}	12	8.6%	1.1%

Although the temperature pre-change (shown in Fig. 3 and 4) will significantly increase the temperature change of microcantilevers $\Delta T_{\rm C}$ in the substrate-free FPA, it is, in other words, the thermal cross talk, which brings out a suspicion that the modulation transfer function (MTF) of the substrate-free FPA will not be particularly good. Here, the MTF is the modulus of the optical transfer function (OTF),[19] which is the Fourier transform of the point spread function. Therefore, the MTF describes the response of an optical system to an image decomposed into sine waves. In other words, the MTF is a measure of the ability for the FPA to transfer contrast from the specimen (maybe IR sources) to the FPA at a specific resolution. Finite element analysis therefore is utilized to present some rough understanding about this. Taking a pixel size of 30×30 μm^2 for example, 10 pW/μm^2 heat fluxes with different spatial resolutions were applied to the FEM, and the temperature distributions obtained are shown in Fig. 6. When the heat flux is at a coarse spatial resolution, the MTF of the substrate-free FPA is particularly good. However, with the increase of spatial resolution, the MTF decreases from excellent to poor. Especially when the heat flux is with a spatial period of two pixels (Fig. 6(d)), the MTF value is only 0.11. It is worth noting that the average temperature change in Fig. 6(d), however, is estimated to be 1.00 K, increasing to about 4.0 times that of the substrate FPA. This means that the substrate-free FPA has an enormous advantage in IR target recognition and an excellent performance for the most common applications, but with a decline in MTF especially when the IR target is at a fine spatial resolution.

On the other hand, the MTF can be improved by further refinement of the supporting frame. Figure 7 shows the merits simulated by decreasing thermal conductance of the supporting frame $G_{\rm frm}$ from infinity (corresponding to the substrate FPA) to zero. With the decrease of thermal conductance $G_{\rm frm}$, not only the thermal cross talk weakens, but also the temperature change $\Delta T_{\rm C}$ increases, which is consistent with the result from expression (4). If $G_{\rm frm}$ could theoretically decrease to zero, there will exist only radiative heat exchange $G_{\rm rad}$. The thermal cross talk therefore can be eliminated completely and the temperature change $\Delta T_{\rm C}$ will reach the maximum limit of 1.78 K. Actually this refinement presents a way to achieve an FPA with smaller pixel size and better performance, because with the decrease of pixel size, the cross sectional area of the supporting frame will usually decrease, and the thermal conductance of the supporting frame $G_{\rm frm}$ therefore will also decrease.

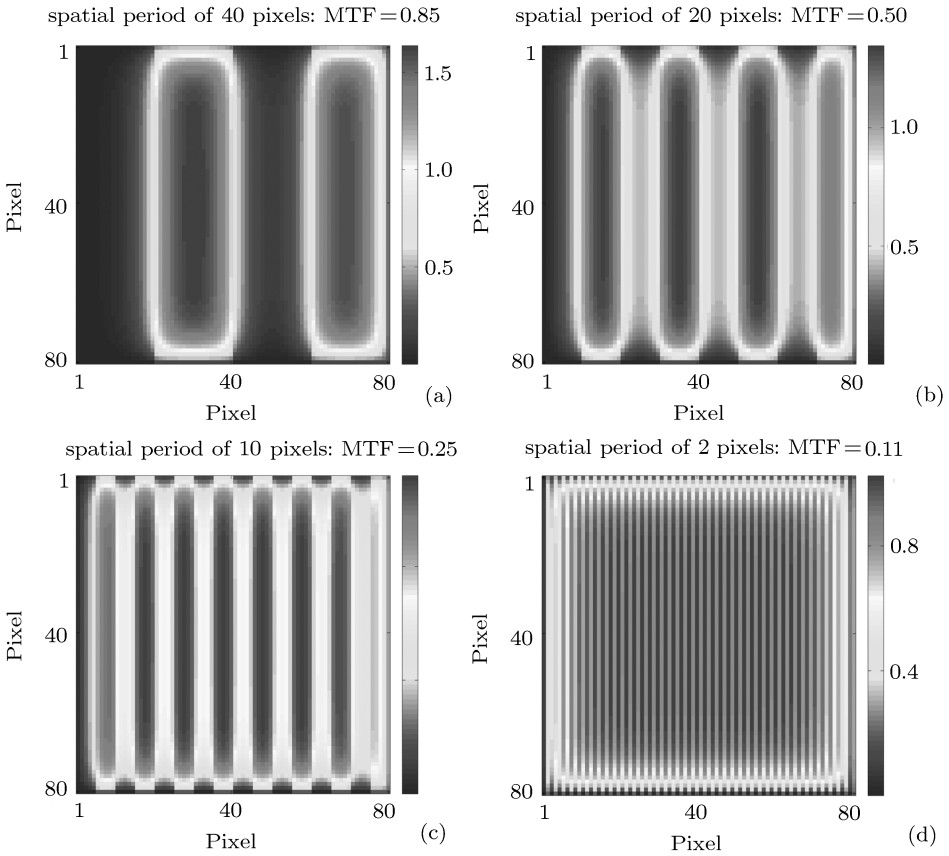


Fig. 6. Temperature distributions (in units of K) caused by the 10 pW/μm^2 heat flux with different spatial resolutions over the substrate-free FPA (with a pixel size of 30×30 μm^2).

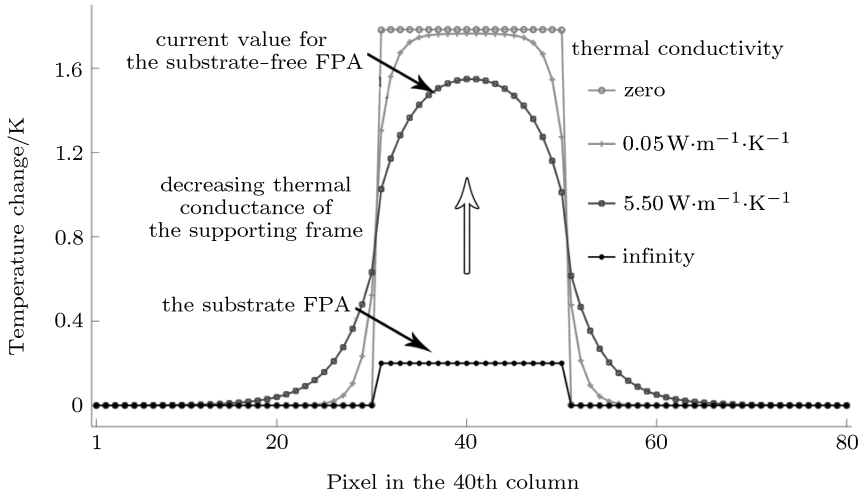


Fig. 7. Temperature distributions in the 40th column of the model simulated by gradually decreasing thermal conductance of the supporting frame. The 3.6 μW (10 pW/μm^2) heat flux is applied to the central area of the model (with a pixel size of 30×30 μm^2).

The thermo-mechanical sensitivity $S_{\rm T}$ is also a key parameter in evaluating the performance of FPAs, and it is defined as the deflection of microcantilevers Δz to the temperature change of microcantilevers $\Delta T_{\rm C}$ (namely, $S_{\rm T} = \Delta z/\Delta T_{\rm C}$). In order to achieve a higher sensitivity, we proposed the two-fold interval-metalized architecture (shown in Fig. 1). Let $S'_{\rm T}$ be the thermo-mechanical sensitivity of only one fold. For the substrate FPA (or the substrate-free FPA but with a small temperature change in the supporting frame as shown in Fig. 5(a)), there is a linear temperature gradient in the thermal isolation region delivering

from the IR absorber to the supporting frame.[14] The temperature change in the second fold is only about 50% of that in the first fold. The thermo-mechanical sensitivity therefore can be evaluated to be $1.5\times S'_{\rm T}$. If the substrate-free FPA, however, has a remarkable temperature change in the supporting frame as shown in Figs. 5(b) and 5(c), the temperature change in the two-fold interval-metalized architecture is almost at a similar value, very close to that in the IR absorber. The thermo-mechanical sensitivity therefore can be evaluated to be $2.0\times S'_{\rm T}$, i.e. it increases by about 33% as compared with the substrate FPA. This inference is well supported by the finite element analysis. By applying the temperature distributions (shown in Fig. 4) obtained from the second kind of thermal load to the FEMs, structural static analysis was then performed, and as a result Fig. 8 shows the deflection distributions of the microcantilever. The largest deflections occur at the ends of the IR absorbers. The values of the corresponding thermo-mechanical sensitivity $S_{\rm T}$ are listed in Table 4. Here, the thermo-mechanical sensitivity $S_{\rm T}$ is calculated by first measuring the perpendicular distance from the tip of the IR absorber to the plane of the FPA and then dividing the measured distance by the corresponding temperature change. In order to be consistent with the previous work, the thermo-mechanical sensitivity is also expressed as a ratio of deflection angle $\Delta\theta$ to temperature change $\Delta T_{\rm C}$. Note that the behaviour of FEM 1 is more similar to that of a substrate FPA, therefore the thermo-mechanical sensitivity $S_{\rm T}$ increases by only 16% as compared with the substrate FPA. For FEMs 2 and 3, the values of thermo-mechanical sensitivity $S_{\rm T}$ increase by about 25% and 31% respectively as compared with those for the substrate FPA.

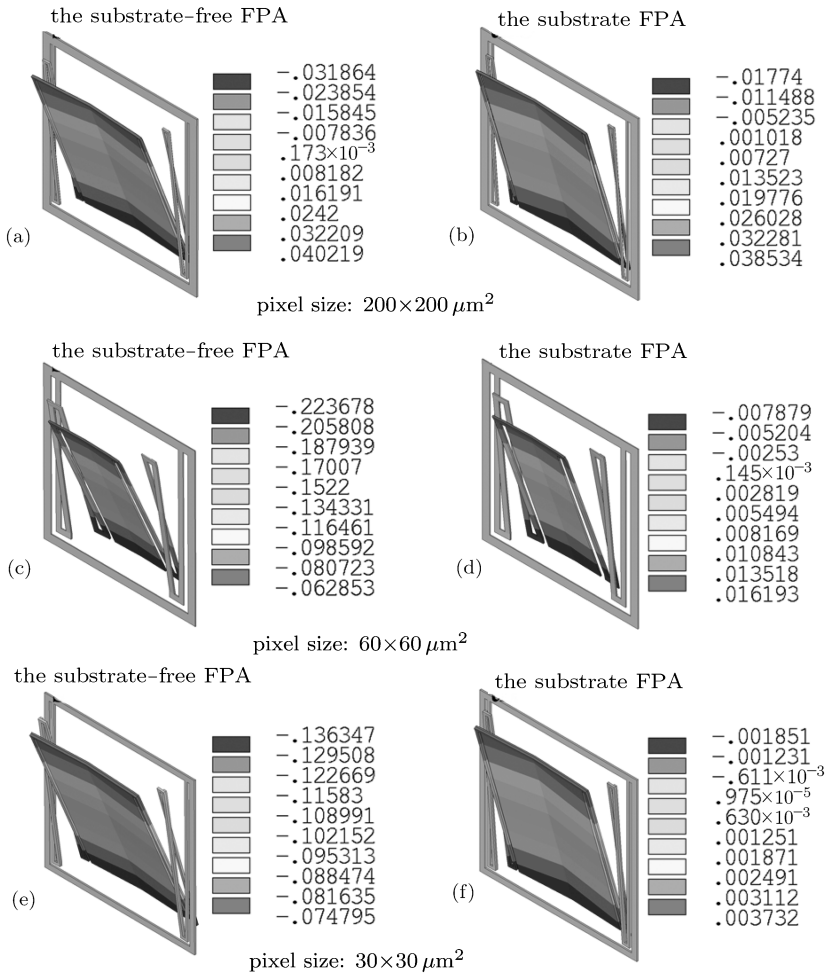


Fig. 8. Deflection distributions of the microcantilevers caused by the temperature distributions shown in Fig. 4.

Table 4. Thermo-mechanical sensitivities of the substrate/substrate-free FPAs obtained by structural static analysis.

model No.	type of the FPA	temperature change $\Delta T_{\rm C}$ /K	deflection Δz /nm	thermo-mechanical sensitivity $S_{\rm T}$ /(nm/K)	/($\times 10^{-3}$ rad/K)
1	substrate-free FPA	1.19	46.9	39.4	0.44
	substrate FPA	1.13	38.5	34.1	0.38
2	substrate-free FPA	1.23	99.7	81.1	3.06
	substrate FPA	0.25	16.2	64.8	2.45
3	substrate-free FPA	1.55	37.5	24.2	1.73
	substrate FPA	0.20	3.7	18.5	1.32

In general, primarily benefiting from the temperature-variable supporting frame, the substrate-free FPA demonstrates an excellent thermal response, which is defined as the deflection angle of microcantilevers $\Delta\theta$ due to the temperature change of IR sources $\Delta T_{\rm S}$ (namely, $H \times S_{\rm T}$). If the thermal conductance of the supporting frame $G_{\rm frm}$ is still relatively large, the behaviour of the substrate-free FPA will be more similar to that of the substrate FPA, and there is no obvious improvement on performance. The thermal response of FEM 1 only increases by about 20% as compared with that of the substrate FPA. However, if the thermal conductance of the supporting frame $G_{\rm frm}$ decreases obviously, the thermal response of the substrate-free FPA will increase significantly. For FEMs 2 and 3, the thermal responses of 2.08×10^{-4} and 1.49×10^{-4} rad/K increase by about 5 and 10 times respectively as compared with those of the substrate FPA.

4. Experiments and results

The finite element analyses, as described above, were validated experimentally by using the substrate-free FPAs with pixel sizes of 200×200 and 60×60 μm^2, which are picked out from the FPAs and have been fabricated successfully.[11−14] Figure 9 shows micrographs of the two FPAs. The array sizes are 100×100 and 160×160 respectively. The material properties and structural parameters used are indicated in Tables 1 and 2.

In order to test their performances, an uncooled infrared detector with optical readout was proposed.[20] It is based on Fraunhofer diffraction. A schematic illustration is shown in Fig. 10. The IR radiation (8–14 μm) from the target is focused onto the FPA by using an IR lens. The incident energy thus causes the temperature of the microcantilevers to increase and, therefore, leads to bending deflections in the bimaterial regions, which is also for the IR absorbers. Simultaneously, the FPA is illuminated by a visible parallel beam on the opposite (a green light-emitting diode (LED) is used in this work). The deflection of individual absorbers is thus proportionally present as a corresponding translation of the diffraction pattern on the back focal plane of the Fourier lens. The required angle-to-intensity

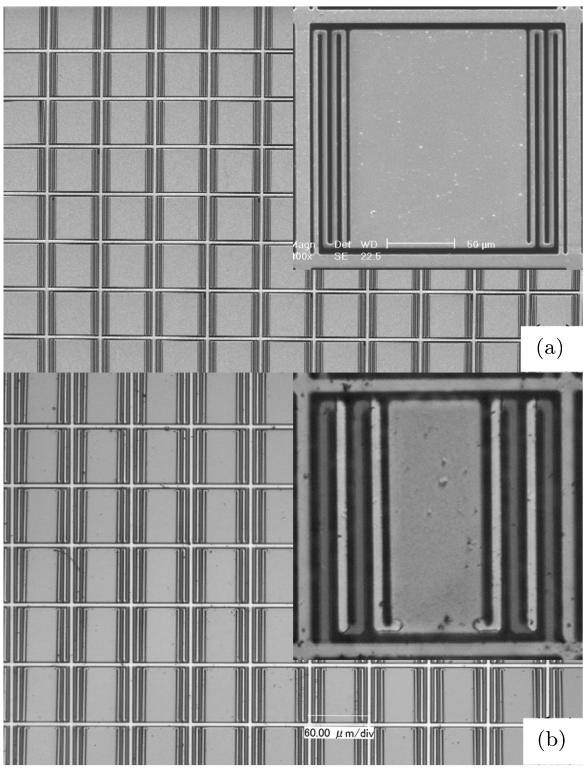


Fig. 9. Micrographs of the substrate-free FPAs with pixel sizes of (a) 200×200 and (b) 60×60 μm^2. The two FPAs are picked out from the FPAs and have been fabricated successfully.

conversion is finally achieved by using a knife-edge fil-

ter, which is located on the back focal plane. As a result, the IR target thermally imaged on the FPA can be reconstructed readily by a CCD camera.

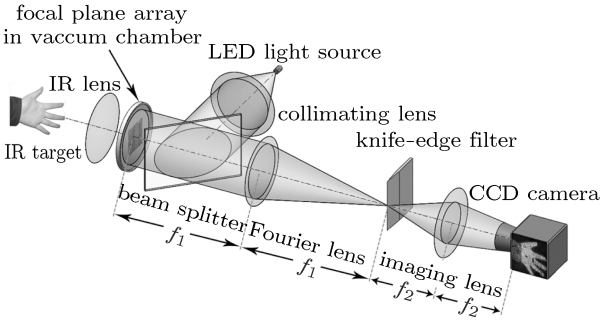


Fig. 10. Schematic illustration of the proposed uncooled IR detector with optical readout.

According to the definition, the NETD can be expressed as

$$\mathrm{NETD} = \frac{I_{\mathrm{noise}}}{\Delta I/\Delta T_{\mathrm{S}}}, \tag{10}$$

where I_{noise} is the grey level of system noise (in this work, $I_{\mathrm{noise}} = 8$ grey levels [14]); $\Delta I/\Delta T_{\mathrm{S}}$ represents the detector sensitivity, which is defined as the ratio of grey-level change of the CCD camera, ΔI, to temperature change of IR source, ΔT_{S}.

Theoretically, the detector sensitivity can be calculated from

$$\frac{\Delta I}{\Delta T_{\mathrm{S}}} = H \times S_{\mathrm{T}} \times \frac{\Delta I}{\Delta \theta}, \tag{11}$$

where $\Delta I/\Delta\theta$ is the optical readout sensitivity, which is defined as the ratio of the grey-level change of the CCD camera, ΔI, to the deflection angle of microcantilevers, $\Delta\theta$. In this work, the optical readout sensitivities were measured experimentally by fixing the FPAs on a stepping motor. By rotating this stepping motor with an accuracy of 0.015°, the relationships between the grey-level change of the CCD camera and the deflection angle of the microcantilevers were obtained and shown in Fig. 11. The slopes, which correspond to the optical readout sensitivities, thus were estimated to be 9870 and 3280 grey levels/degree respectively. Based on Eq. (11), the detector sensitivities of the selected FPAs can thus be calculated to be 16 ($=6.6\%\times0.44\times10^{-3}\times9870\times180/\pi$) and 39 ($=6.8\%\times3.06\times10^{-3}\times3280\times180/\pi$) grey levels/K respectively. In contrast, if substrate FPAs with pixel sizes 200×200 and 60×60 μm^2 are implemented, the detector sensitivities can be predicted to be 14 ($=6.3\%\times0.38\times10^{-3}\times9870\times180/\pi$) and 6 ($=1.4\%\times2.45\times10^{-3}\times3280\times180/\pi$) grey levels/K respectively. With the decrease of pixel size, the advantage of the substrate-free FPA becomes more and more prominent.

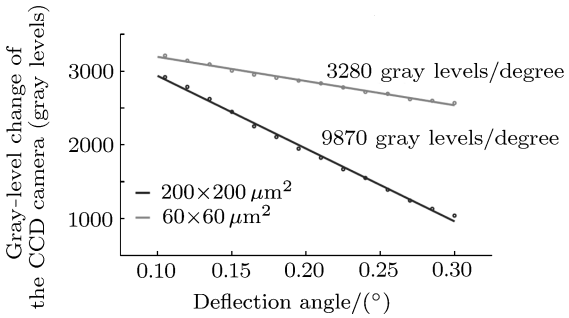


Fig. 11. Optical readout sensitivities experimentally measured by rotating the stepping motor with an accuracy of 0.015°.

The detector sensitivities of the selected FPAs were also measured experimentally by using a calibrated blackbody source. By gradually increasing the temperature of the blackbody source with a step of 2 K from 25 to 39 K, the relationships between the grey-level change of the CCD camera and the temperature change of the blackbody source were obtained. Histograms of the detector sensitivities are shown in Fig. 12. The experimentally measured values of 15.5 and 27.2 grey levels/K are consistent with the theoretical predictions. The difference between the values

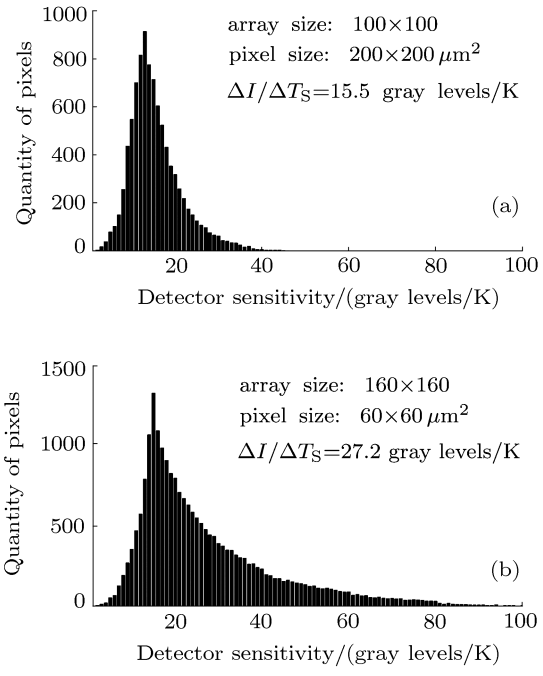


Fig. 12. Histograms of the detector sensitivity obtained by gradually increasing the temperature of the blackbody source from 25 K to 40 K.

39 and 27.2 grey levels/K is mainly induced by the non-uniformity of the initial deflection angle. As can be seen in Fig. 12(b), only a relatively small portion of the microcantilevers has an efficiency close to optimal efficiency, where the microcantilevers are characterized by the detector with a sensitivity of 50 grey levels/K or more. Finally, based on expression (10), the NETD values of the selected FPAs were estimated to be 520 and 300 mK respectively.

Examples of thermal images obtained are displayed in Fig. 13. The upper images were obtained by the FPA with a pixel size of 200×200 μm^2, and the lower images were obtained by the FPA with a pixel size of 60×60 μm^2. Obviously the latter demonstrates a better imaging performance.

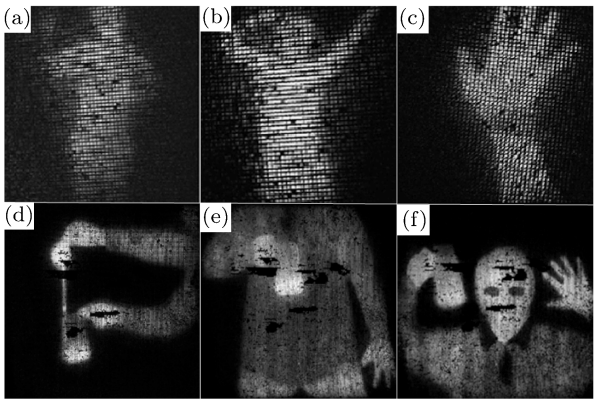


Fig. 13. Thermal images obtained by the selected FPAs with pixel sizes of 200×200 ((a)–(c)) and 60×60 μm^2 ((e), (f)).

5. Discussion

The imaging performance of the proposed IR detector is seriously limited by the optical readout sensitivity. For pixel sizes of 200×200 and 60×60 μm^2, the optical readout sensitivities can be theoretically estimated to be 50000, and 15000 grey levels/degree respectively.[13,14] As can be seen in Fig. 11, however, the optical readout sensitivities experimentally determined are only one fifth of the theoretical predictions. This is induced mainly by the undesired deformations in the IR absorbers.[21] On the other hand, a remarkable improvement is achieved by improving the optical readout sensitivity. The undesired deformations, caused by stress mismatch in the bilayer structure, may be eliminated, for instance, by embedding stiffeners in the IR absorbers. In addition, it would also be beneficial to employ the annealing technique to minimize the film stress. If the optical readout sensitivity can thus be significantly improved, the selected FPAs have a potential of achieving NETD values of 100 and 45 mK respectively.

The intrinsic performance of the substrate-free FPA can be improved by refining the FPA geometry and using materials with coefficients of thermal expansion very different from each other, namely Al and SiO_2. According to Fig. 7, it would be beneficial to the reducing of the thickness of the structural material (SiN_x or SiO_2). A higher thermo-mechanical sensitivity can be achieved by employing the three-fold interval-metalized architecture or optimizing the thickness ratio in the bilayer structure. To enhance the detector IR absorption, an appropriate resonance cavity can be embedded into the IR absorber. Meanwhile, work by Grbovic *et al.* has demonstrated microfabrication by using the materials Al and SiO_2.[22] For the FPA with a pixel size of 30×30 μm^2 for instance, finite element analysis shows that if the refinements described above can be performed successfully (by employing the three-fold interval-metalized architecture; by using the materials Al and SiO_2 and then by optimizing the thicknesses to be 0.08 and 0.1 μm respectively), an NETD value of 10 mK can be achieved.

6. Conclusions

The thermal and mechanical characterizations of the substrate-free FPA are investigated. Because of the large decrease in thermal conductance, the supporting frame is temperature dependent, which brings out a unique thermal characteristic, i.e. the lower the thermal conductance of the supporting frame is, the higher the energy conversion efficiency in the substrate-free FPA will be. The decreasing trend in the substrate FPA, namely that the energy conversion efficiency decreases with decreasing pixel size, is completely avoided. Meanwhile, a potential of 33% improvement in thermo-mechanical sensitivity is also achieved. With the decrease of pixel size, the thermal and mechanical characterizations of the substrate-free FPA become more and more prominent. For an FPA with a pixel size of 200×200 μm^2, the thermal conductance of the supporting frame is still relatively large, the temperature of the supporting frame therefore varies slightly, and the thermal response only increases by about 20% as compared with that of the substrate FPA. However, for FPAs with pixel sizes of 60×60 and 30×30 μm^2, the thermal conductances of the supporting frames are decreased greatly, the temperatures of the supporting frames therefore vary significantly,

and the thermal responses therefore increase by about 5 and 10 times respectively. The results from the finite element analyses are consistent with our measurements: two types of substrate-free FPAs with pixel sizes of 200×200 and 60×60 μm^2, picked out from the fabricated FPAs, were implemented in the proposed IR detector. The NETD values are experimentally measured to be 520 and 300 mK respectively. Further refinements are achieved in various aspects, including the optical readout sensitivity, the FPA geometry, and the materials used. If these refinements can be realized successfully, the substrate-free FPA with a pixel size of 30×30 μm^2 has a potential application to achieving an NETD value of 10 mK.

Acknowledgement

The authors would like to thank Prof. He Linghui for his valuable discussion.

References

[1] Lloyd J M 1975 *Thermal Imaging Systems* (New York: Plenum Press)

[2] Miller J L 1994 *Principles of Infrared Technology* (New York: Cluwer Academic Pub)

[3] Rogalski A 2003 *Infrared Detectors: Status and Trends* In: *Prog. Quant. Electron.* **27** p59

[4] Li B 2004 *Sensor Actuat.* A **112** 351

[5] Boisen A, Thaysen J, Jensenius H and Hansen O 2000 *Ultramicroscopy* **82** 11

[6] Gotszalk T, Grabiec P and Rangelow I W 2000 *Ultramicroscopy* **82** 39

[7] Manalis S R, Minne S C, Quate C F, Yaralioglu G G and Atalar A 1997 *Appl. Phys. Lett.* **70** 3311

[8] Perazzo T, Mao M, Kwon O and Majumdar A 1999 *Appl. Phys. Lett.* **74** 3567

[9] Zhao Y, Mao M, Horowitz R, Majumdar A, Varesi J, Norton P and Kitching J 2002 *J. Microelectromech.* S **11** 136

[10] Grbovic D, Lavrik N V, Datskos P G, Forrai D, Nelson E, Devitt J and McIntyre B 2006 *Appl. Phys. Lett.* **89** 073118

[11] Pan L, Zhang Q C, Wu X P, Duan Z H, Chen D P, Wang W B and Guo Z Y 2004 *J. Experimental Mechanics* **19** 403 (in Chinese)

[12] Li C B, Jiao B B, Shi S L, Chen D P, Ye T C, Zhang Q C, Guo Z Y, Dong F L and Miao Z Y 2006 *Meas. Sci. Technol.* **17** 1981

[13] Miao Z Y, Zhang Q C, Chen D P, Guo Z Y, Dong F L, Xiong Z M, Wu X P, Li C B and Jiao B B 2007 *Ultramicroscopy* **107** 640

[14] Dong F L, Zhang Q C, Chen D P, Miao Z Y, Xiong Z M, Guo Z Y, Li C B, Jiao B B and Wu X P 2008 *Ultramicroscopy* **108** 579

[15] Kruse P W 1997 *Principles of Uncooled Infrared Focal Plane Arrays* In: *Semiconduct. Semimet.* **47** p17

[16] Zhao Y 2002 *Optomechnical Uncooled Infrared Imaging System* Ph. D Thesis, University of California, Berkeley, USA

[17] Xiong Z M, Zhang Q C, Gao J, Wu X P, Chen D P and Jiao B B 2007 *J. Appl. Phys.* **102** 113524

[18] Wood R A 1997 *Monolithic Silicon Microbolometer Arrays* In: *Semiconduct. Semimet.* **47** p43

[19] Goodman J W 2006 *Introduction to Fourier Optics* 2nd Ed. (New York: McGRAW-HILL) p139

[20] Duan Z H, Zhang Q C, Wu X P, Pan L, Chen D P, Wu X P and Guo Z Y 2003 *Chin. Phys. Lett.* **20** 2130

[21] Miao Z Y, Zhang Q C, Guo Z Y, Wu X P and Chen D P 2007 *Opt. Lett.* **32** 594

[22] Grbovic D, Lavrik N V, Rajic S and Datskos P G 2008 *J. Appl. Phys.* **104** 051508